*International Society for Rock Mechanics and Rock Engineering*
*Macedonian Association for Geotechnics*

*ISRM Regional Symposium*
*Eurock 2026*
*Risk Management in Rock Engineering*
*Skopje, 15-19 September*

DOI: https://doi.org/10.68732/2a51bc6270fd2755

ISBN: 978-9989-2053-7-8

# Hydro-mechanical coupled behaviors of weakly cemented sandstones during two-phase fluids displacement: insights from a micro-continuum VOF-BPM method

Shihang Chen & Fengshou Zhang
*Tongji University, Shanghai, China*
fengshou.zhang@tongji.edu.cn

## Abstract

Geological $CO_2$ storage (GCS) aims to permanently reduce carbon emissions by injecting supercritical $CO_2$ ($scCO_2$) or water-$CO_2$ into subsurface formations. Weakly cemented sandstones, which are widely distributed within saline aquifers, represent one of the primary storage media. However, the coupled hydro-mechanical behaviors of these formations during two-phase fluid displacement remain largely unexplored, despite significantly impacting the efficiency and safety of GCS.

In this study, a micro-continuum VOF-BPM method is proposed to accurately capture the complex hydro-mechanical interactions between weakly cemented sandstones and two-phase fluids. An intra-particle porosity is first defined to transform single particles into permeable discrete elements, and the rock's mechanical behavior is simulated using the Bonded Particle Model (BPM). Simultaneously, the Volume of Fluid (VOF) algorithm, the micro-continuum method, and the two-phase Darcy model are fully coupled to resolve multiscale flow through fractures and the matrix.The newlyproposed Semi-Implicit Hydro-Mechanical (SIHM) coupling algorithm introduces an elastic concept into DEM-based fluid-solid coupling, enabling a coordinated solution of fluid volume expansion and solid deformation.

A quasi-2D model is built to simulate $scCO_2$ injection into weakly cemented sandstones under varied conditions. Results show that in high-permeability sandstones, increased injection rates trigger a rapid transition from matrix seepage to fracture propagation, revealing a clear flow-path competition. Unstable displacement fronts within the matrix, governed by the small viscosity ratio between invading and defending fluids, are also well captured. Such instability and flow-path competition strongly shape the final $CO_2$ distribution, affecting overall storage efficiency. These findings underscore that accurate fracture prediction in high-permeability reservoirs necessitates a precise characterization of two-phase displacement dynamics, demonstrating the advanced capability of the proposed micro-continuum VOF-BPM method and providing critical insights for optimizing GCS operations.

## Keywords

CFD-DEM, Hydraulic fracturing, Micro-continuum, Sandstone.

# 1 Introduction

Geological $CO_2$ storage (GCS) is a key strategy for mitigating climate change and supporting a sustainable energy transition, and its effectiveness depends on complex interactions between multiphase fluids and discrete porous media(Snæbjörnsdóttir et al., 2020).Weakly cemented, high-permeability sandstones commonly serve as major sequestration reservoirs. In such formations, $CO_2$injection behavior is strongly controlled by heterogeneous mechanical and seepage characteristics. Understanding the mesoscale coupling between fracture propagation and matrix seepage is therefore essential for improving storage efficiency and ensuring long-term safety.

Existing numerical methods can be broadly divided into continuum and discrete approaches. Continuum models capture engineering-scale hydraulic fracturing but struggle to resolve coupled fluid displacement and fracture evolution in highly heterogeneous, discrete media. Discrete approaches, such as coupled Pore Network Model (PNM) and Discrete Element Method (DEM)(Li et al., 2024), better represent mesoscale interfaces. However, they often rely on Poiseuille-flow assumptions and simplified leak-off models. These limitations restrict their applicability to two-phase fluids flow in fractured porous media. Conventional coupling of DEM and Computational Fluid Dynamics (CFD) coupling solves the Navier-Stokes equations. Yet, its loosely coupled fluid-solid interaction is generally insufficient to simulate fracture initiation and propagation(Kazidenov and Amanbek, 2025).

To address these challenges, this study develops a micro-continuum VOF-BPM framework. The frameworkinnovatively integrates the Volume of Fluid (VOF) method, the Bonded Particle Model (BPM)(Potyondy and Cundall, 2004), and micro-continuum theory(Soulaine and Tchelepi, 2016). A Semi-Implicit Hydro-Mechanical (SIHM) coupling algorithm is introducedfor the first time by incorporating elasticity into the coupling strategy. This enables accurate mesoscale interaction between two-phase fluids and discrete porous media. Finally, a hydraulic fracturing model considering mechanical heterogeneity is established to demonstrate the robustness and computational capabilities of the proposed method.

# 2 Micro-continuum VOF-BPM framework

The micro-continuum VOF–BPM framework is developed on the open-source CFDEM platform (Goniva et al., 2012), which couples OpenFOAM for CFD with LIGGGHTS for DEM. This section introduces the BPM formulation and the governing equations of micro-continuum theory. A semi-implicit coupling algorithm is then introduced to couple fluid pressure with solid elastic deformation. This framework enables accurate mesoscale simulation of hydraulic fracture propagation under two-phase fluid displacement.

## 2.1 The bonded particle model

The Bonded Particle Model (BPM) represents rock by connecting discrete particles with bonds and has been widely used in hydraulic fracturing studies. In this work, BPM is implemented in LIGGGHTS(Schramm et al., 2019). Particle motion is governed by forces and moments arising from inter-particle contacts and cementitious bonds. The inter-particle contact interactions are described by the Hertzian contact model, whereas the force-displacement law of the bonds is given as follows:

$$\begin{aligned} \Delta \mathrm{F_n} &= \mathrm{K}_n A_b \dot{x}_n \Delta \mathrm{t} \\ \Delta \mathrm{F}_t &= \mathrm{K}_t A_b \dot{x}_t \Delta \mathrm{t} \\ \Delta \mathrm{M}_n &= \mathrm{K}_t J_b \dot{\theta}_n \Delta \mathrm{t} \\ \Delta \mathrm{M}_t &= \mathrm{K}_n I_b \dot{\theta}_t \Delta \mathrm{t} \end{aligned} \tag{1}$$

where $\Delta \mathrm{F_n}$ and $\Delta \mathrm{M}_n$are the increments of normal force and moment carried by the bond, and$\Delta \mathrm{F}_t$and $\Delta \mathrm{M}_t$are the increments of tangential force and moment.$A_b$, $J_b$and $I_b$are thebond cross-sectional area, polar moment of inertia, and moment of inertia, respectively, assuming a cylindrical bond geometry. The normal and tangential stiffness per unit area are defined as $K_n = E_b/l_b$ and $K_t = G_b/l_b$where with $E_b$ and $G_b$ are the elastic and shear moduli .c The bond radius is defined as $R = \lambda \min(R_A, R_B)$, where $R_A$ and $R_B$ are the radii of the bonded particles, and $\lambda$ is the radius multiplier. In this study, $\lambda = 1$.Then the maximum normal stress $\sigma$ and tangential stress $\tau$ acting on the bond periphery are then obtained as:

$$\sigma = -\frac{\mathrm{F_n}}{A_b} + \frac{|M_t|R}{I_b} \tag{2}$$

$$\tau = \frac{|\mathrm{F}_t|}{A_b} + \frac{|M_n|R}{J_b}$$

The bond will break only when$\sigma \geq \sigma_c$ or $\tau \geq \tau_c$, where $\sigma_c$and $\tau_c$are normal and tangential strength of the bond. Here, $F_n > 0$ corresponds to bond compression(Potyondy and Cundall, 2004).

## 2.2 The micro-continuum method

In this work, an intra-particle porosity$n$is introduced to upscale a DEM particle from a single grain to a discrete porous mechanical element. This treatment fundamentally alters particle-fluid interactions. Fluid flow inside the particle is modelled as matrix seepage with $n_s < n < 1$whereas flow outside the particle is treated as free flow with$n = 1$, where $n_s$denotes minimum intra-particle porosity. The porosity $n$ is further naturally linked to the void fraction $\phi_s$obtained in solid volume mapping in conventional resolved CFD-DEM methods.

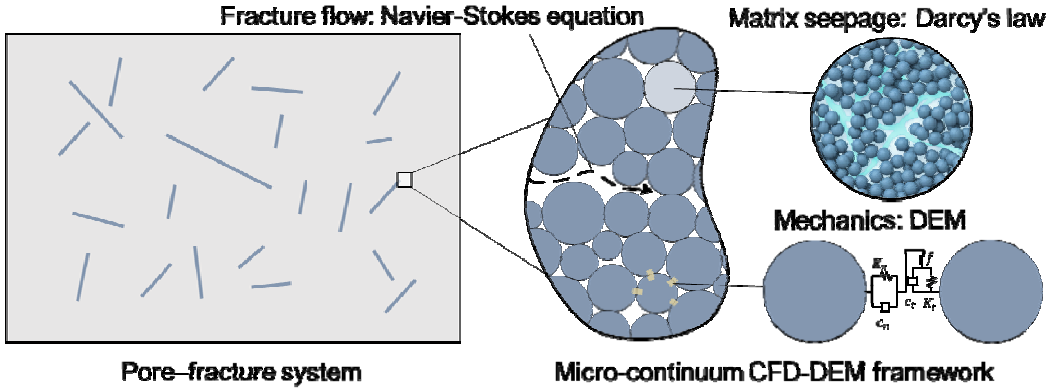



Fig. 1 Schematic illustration of the micro-continuum CFD–DEM coupling framework.

Then, the micro-continuum method, a unified model for matrix seepage and free flow, is employed and the governing equations are formulated as:

$$\frac{1}{n}\cdot\frac{\partial(\rho_f \boldsymbol{U_f})}{\partial t} + \frac{1}{n}\nabla\cdot\left(\frac{\rho_f}{n}\boldsymbol{U_f}\otimes\boldsymbol{U_f}\right) = -\nabla p + \nabla\cdot\left(\frac{\mu_f}{n}\nabla\otimes\boldsymbol{U_f}\right) + \boldsymbol{F_c} + \rho_f\boldsymbol{g} + \frac{\mu}{K}\left(\boldsymbol{U_s} - \boldsymbol{U_f}\right) \tag{3}$$

$$\frac{\partial n}{\partial t} + \nabla\cdot\boldsymbol{U_f} = 0 \tag{4}$$

where $\boldsymbol{U_f}$is the fluid velocity,$p$is the pressure,$\boldsymbol{g}$is gravitational acceleration, and $\boldsymbol{U_s}$is the particle velocity. $\rho_f$and $\mu_f$denote the fluid density and viscosity, respectively. The VOF method is employed to capture the two-phase interface with a volume fraction of wetting phase$\alpha_w$and of non-wetting phase $\alpha_n$,with $\alpha_w + \alpha_n = 1$. Specifically, $\alpha_w = 1$ in the wetting phase and $\alpha_w = 0$ in the non-wetting phase,while $0 < \alpha_w < 1$ indentifies the interface position.Fluid properties are then evaluated accordingly.

$$\rho_f = \alpha_w\rho_w + \alpha_n\rho_n \tag{5}$$

$$\mu_f = \alpha_w\mu_w + \alpha_n\mu_n \tag{6}$$

And the evolution of $\alpha_w$is governed by the phase equation:

$$\frac{\partial \alpha_w n}{\partial t} + \nabla\cdot\left(\alpha_w\boldsymbol{U_f}\right) + \nabla\cdot\left(n\alpha_w a_n\boldsymbol{U_r}\right) = 0 \tag{7}$$

The third term on the LHS of Eq. (5) accounts for interface compression, with $\boldsymbol{U_r}$being the relative velocity between the two fluid phases, defined differently in solid and solid-free regions.

The fluid-particle momentum exchange is formualted with $\frac{\mu}{K}\left(\boldsymbol{U_s} - \boldsymbol{U_f}\right)$given the porous media representation of particles. While the Continuum Surface Force (CSF) model computes surface tension force term $\boldsymbol{F_c}$ and $\boldsymbol{U_r}$ in solid-free regions, the two-phase Darcy model is used inside porous media(Carrillo et al., 2020).The resulting formulations are given below.

$$\frac{\mu}{K} = \begin{cases} 0 & n = 1 \\ k_0^{-1}\left(\frac{k_{r,w}}{\mu_w} + \frac{k_{r,n}}{\mu_n}\right)^{-1} & n < 1 \end{cases} \tag{8}$$

$$\boldsymbol{F_c} = \begin{cases} \sigma_s k \nabla \alpha_w & n = 1 \\ M^{-1}(M_w \alpha_n - M_n \alpha_w)[(\rho_w - \rho_n)\boldsymbol{g} + \nabla p_c] - p_c \nabla \alpha_w & n < 1 \end{cases} \tag{9}$$

$$\boldsymbol{U_r} = \begin{cases} C_\alpha \max\left(|\boldsymbol{U_f}|\right) \nabla \alpha_w & n = 1 \\ \frac{1}{n}[-\left(\frac{M_w}{\alpha_w} - \frac{M_n}{\alpha_n}\right)\nabla p + \left(\rho_w \frac{M_w}{\alpha_w} - \rho_n \frac{M_n}{\alpha_n}\right)\boldsymbol{g} + \\ \left(\frac{M_w \alpha_n}{\alpha_w} + \frac{M_n \alpha_w}{\alpha_n}\right)\nabla p_c - \left(\frac{M_w}{\alpha_w} - \frac{M_n}{\alpha_n}\right) p_c \nabla \alpha_w] & n < 1 \end{cases} \tag{10}$$

Here, $\sigma_s$is the surface tension coefficient, andinterface curvature $k$ is computed from the unit normal vector $\boldsymbol{n_i}$ as $k = -\nabla \cdot \boldsymbol{n_i} = -\nabla \cdot \frac{\nabla \alpha_w}{|\nabla \alpha_w|}$.The interface compression coefficient$C_\alpha$is set to 1.0 in this study.The absolute permeability is defined as$k_0 = k_{0,s}\frac{n^3}{(1-n)^2}\frac{(1-n_s)^2}{n_s^3}$is,where $k_{0,s}$is the reference permeability. $k_{r,i}$and $M_i$are the relative permeability and mobility of phase $i$, respectively, with $M_i = \frac{k_{r,i}k_0}{\mu_i}$.The total mobility is $M = M_w + M_n$. The van Genuchten model is adopted(Van Genuchten, 1980),with$k_{r,i}$depending on the effective saturation $\alpha_{w,eff}$.

$$k_{r,w} = \left(1 - \alpha_{w,eff}\right)^{\frac{1}{2}}\left(1 - \alpha_{w,eff}^{\frac{1}{m_p}}\right)^{2m_p} \tag{11}$$

$$k_{r,n} = \alpha_{w,eff}^{\frac{1}{2}}\left(1 - \left(1 - \alpha_{w,eff}^{\frac{1}{m_p}}\right)^{m_p}\right)^2 \tag{12}$$

$$\alpha_{w,eff} = \frac{\alpha_w - \alpha_{w,irr}}{1 - \alpha_{n,irr} - \alpha_{w,irr}} \tag{13}$$

where $\alpha_{w,irr}$and $\alpha_{n,irr}$are irreducible saturations of wetting and non-wetting phases.The capillary pressure $p_c$is a function of normalized wetting phase saturation $\alpha_{w,pc}$defined by$\alpha_{w,pc} = \frac{\alpha_w - \alpha_{pc,irr}}{\alpha_{pc,max} - \alpha_{pc,irr}}$, where$\alpha_{pc,max}$and $\alpha_{pc,irr}$are the maximum and irreducible saturationsin capillary model:

$$p_c = p_{c,0}\left(\alpha_{w,pc}^{-\frac{1}{m_p}} - 1\right)^{1-m_p} \tag{14}$$

Here $p_{c,0}$is the entry pressure and $m_p$is a dimenionless number related to the porous media property.

## 2.3 The semi-implicit hydro-mechanical coupling algorithm

In conventional CFD-DEM methods, the staggered fluid-particle solution strategy restricts the time derivative of porosity induced by particle motion to an explicit evaluation. And fluid pressure and porosity evolution are solved in a decoupled manner. As a result, the seepage pressure gradient is reached instantaneously when solid system is highly constraint, where$\frac{\partial n}{\partial t} = \frac{\partial n_v}{\partial t} = 0$.This limitation calls for a more rigorous formulation of porosity evolution at the grid scale for each time step.

During hydraulic fracturing in low-permeability reservoirs, injecting pressure first increases before crack initiation. The increased fluid volume is mainly accommodated through localized solid deformation, which gives rise to enlarged pore spaces. After crack initiation and propagation, additional flow space is created. Consequently, injection pressure decreases under constant flow-rate conditions. Motivated by this physical process, elastic deformation is incorporated into the continuity equation. The time derivative of porosity is decomposed into contributions from particle motion and elastic strain. In this study, the rock matrix itself is assumed incompressible. Overall deformation and pore pressure response of the rock are entirely controlled by the compressibility of the pore space. Accordingly, the Biot's coefficient $\alpha = 1 - \frac{K_b}{K_s} = 1$, where $K_b$is the drained bulk modulus and $K_s$is the intrinsic bulk modulus of solid phase. And $\frac{\partial n}{\partial t}$can be formulated as below (Parisio et al., 2019):

$$\frac{\partial n}{\partial t} = (1-n)\left(\frac{1}{K_s}\frac{\partial p}{\partial t} - \frac{\partial \epsilon_v}{\partial t}\right) \tag{15}$$

where $\epsilon_v$denotes the volumetric strainof solid in one fluid grid due to particle motion:

$$\epsilon_v(t) = \frac{\Delta V_s(t)}{V_s(t)} = \frac{V_s(t) - V_s(0)}{V_s(t)} \tag{16}$$

$$(1-n)\frac{\partial \epsilon_v}{\partial t} = \frac{1}{\Delta t}(1-n)\left(\frac{V_s(t) - V_s(0)}{V_s(t)} - \frac{V_s(t-1) - V_s(0)}{V_s(t-1)}\right) \tag{17}$$

For simplicity, we assume that the volume change from particle velocity is small during each time step which is acceptable in rock deformation, and $\frac{V_s(t-1)-V_s(0)}{V_s(t-1)} \approx \frac{V_s(t-1)-V_s(0)}{V_s(t)}$. Then the Eq. 15 is further derived as:

$$(1-n)\frac{\partial \epsilon_v}{\partial t} = \frac{1}{\Delta t}\frac{V_s(t)}{V}\frac{V_s(t) - V_s(t-1)}{V_s(t)} = \frac{1}{\Delta t}\frac{V_s(t) - V_s(t-1)}{V} = -\frac{\partial n_v}{\partial t} \tag{18}$$

where $V$ is the volume of fluid grid, $\frac{\partial n_v}{\partial t}$is the porosity change due to particle motion and can beobtained from solid volume mapping. To this end, the overall porosity change can be formulated in a semi-implicit way:

$$\frac{\partial n}{\partial t} = (1-n)\frac{1}{K_s}\frac{\partial p}{\partial t} + \frac{\partial n_v}{\partial t} \tag{19}$$

The pressure term is discretized implicitly and the porosity change due to particle motion is solved explicitly.And the continuity equation becomes:

$$(1-n)\frac{1}{K_s}\frac{\partial p}{\partial t} + \frac{\partial n_v}{\partial t} + \nabla \cdot \boldsymbol{U_f} = 0 \tag{20}$$

Therefore, the fluid pressure and velocity can be accurately calculated through solving Eq. 3 and Eq.20. Then the fluid-particle interaction forces acting on each particle is obtained by integrating the fluid stress over particle domain $\Omega_s$:

$$F_f = \int_{\Omega_s} (1-\phi_s)\left(-\nabla p + \mu_f \Delta \boldsymbol{U_f}\right) dV \tag{21}$$

$$M_f = \int_{\Omega_s} \boldsymbol{r} \times (1-\phi_s)\left(-\nabla p + \mu_f \Delta \boldsymbol{U_f}\right) dV \tag{22}$$

And the motion of particles can be determined by Newton's laws, incorporating forces from the fluid, interparticle bonds, and direct contact.

This proposed Semi-Implicit Hydro-Mechanical (SIHM) coupling algorithm enables, for the first time, the coupled solution of fluid pressure and solid deformation within a CFD-DEM framework, making it possible to model rock hydraulic fracturing using a micro-continuum-based CFD-DEM approach.

# 3 Numerical simulations

Fracture propagation and fluid displacement in weakly cemented sandstones play a key role in $CO_2$sequestration, yet their mesoscale mechanisms remain unclear. Based on the micro-continuum VOF–BPM framework presented in Section 2, a numerical model is developed in Section 3.1. The temporal competition between fracture propagation and fluid infiltration during $scCO_2$ injection is investigated in Section 3.2, followed by an analysis of the effects of injection rate and fluid viscosity in Section 3.3.

## 3.1 Baseline test

A quasi-2D fluid domain (15 cm × 5 cm × 0.2 cm) is constructed with a central cylindrical inlet of 0.8 cm diameter, through which $scCO_2$ is injected at a constant velocity (Fig. 2a). A constant-pressure boundary is imposed at the outer boundary, with both the outlet and initial pore pressure set to 10 MPa. The $scCO_2$ is treated as an incompressible fluid with constant properties; compressibility effects are beyond the scope of this study and will be addressed in future work.The fluid domain is discretized using a single-layer mesh of 67,324 cells, with cell size maintained below one-sixth of the minimum particle diameter.

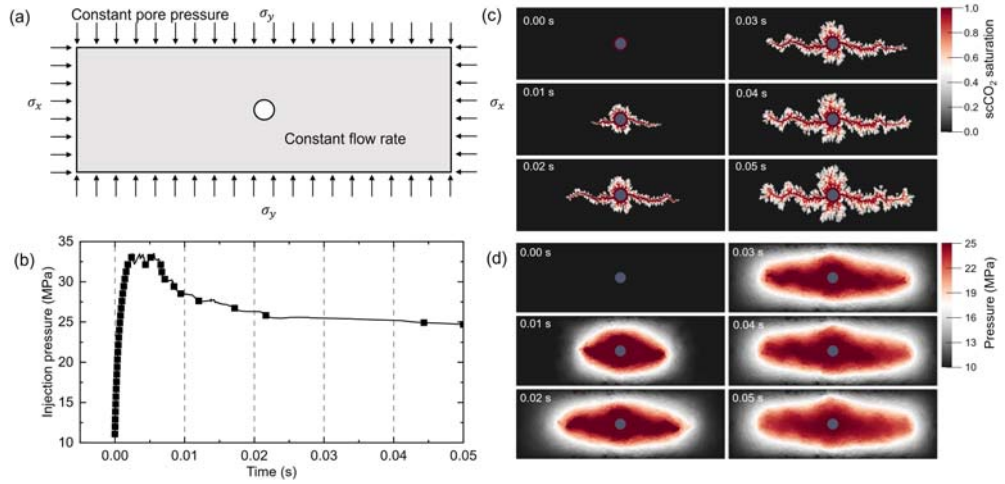



Fig. 2(a) Model configuration; (b) temporal evolution of injection pressure; (c) evolution of $scCO_2$ saturation distribution; (d) evolution of the pore pressure field.

The concentric solid domain (30 cm × 10 cm × 0.2 cm) is subjected to stress-controlled boundaries, with effective stresses of $\sigma_x$=15 MPa and $\sigma_y$=5 MPa, favoring fracture propagation parallel to the x-direction. Solid particles outside the fluid domain provide compliant servo control to reduce boundary effects. More detailed parameters for fluid and solid are presented in Table 1.

Table 1. Summary of model parameters.

| **Model parameters** | | |
|---|---|---|
| Particles | Particle number | 3984 |
| | Density | 2000 kg/m$^3$ |
| | Interparticle friction coefficient | 0.7 |
| | Young's modulus | 1.0 GPa |
| | Poisson's ratio | 0.15 |
| | Particle radius (uniform fraction distribution) | 1.020,1.073,1.147,1.220,1.293 mm |
| Bonds | Elastic modulus, $E_b$ | 1.0GPa |
| | Shear modulus, $G_b$ | 0.3846 GPa |
| | Normal strength, $\sigma_c$ | 10.0 MPa |
| | Tangential strength, $\tau_c$ | 10.0 MPa |
| Fluid | Defending fluid (water) viscosity, $\mu_w$ | 1.0e-3 Pa·s |
| | Defending fluid (water) density, $\rho_w$ | 1000 kg/m$^3$ |
| | Invading fluid ($scCO_2$) viscosity, $\mu_n$ | 5.21e-5 Pa·s |
| | Invading fluid ($scCO_2$) density, $\rho_n$ | 666.63 kg/m$^3$ |
| | Surface tension coefficient, $\sigma_s$ | 0.03 N/m |
| | Injection rate | 0.3 m/s |
| Porous media | Reference permeability, $k_{0,s}$ | 2.0e-14 m$^2$ |
| | Minimum intra-particle porosity, $n_s$ | 0.3 |
| | Irreducible saturation, $\alpha_{i,irr}$ | 0.0 |
| | Entry capillary pressure, $p_{c,0}$ | 0 Pa |
| | van Genuchten model coefficient, $m_p$ | 0.99 |
| | Intrinsic bulk modulus, $K_s$ | 0.4762 GPa |

## 3.2 Competing between fracturing and infiltration

Fig. 2b shows thetemporal evolution of injection pressure. The pressure rises rapidly from the initial pore pressure and reaches a peak of 33.5 MPa. During this stage, the monotonic pressure buildup results from the coordinated response of solid deformation and fluid injection, demonstrating the effectiveness of the proposed SIHM coupling algorithm. After fracture initiation, newly opened flow pathways cause a rapid pressure drop, followed by stabilization at approximately 0.025 s, consistent with the evolution of $scCO_2$saturation shown in Fig. 2c. At early injection stages, fracture length increases rapidly, accompanied by a pronounced rise in $scCO_2$ saturation along the fracture direction, whereas fluid penetration perpendicular to the fracture remains limited. After ~0.03 s, fracture growth slowsmarkedly.$scCO_2$ transport then becomes controlled by matrix infiltration rather than fracture propagation. The enlarged seepage boundary created by fracture growth facilitates pressure dissipation through matrix flow, leading to a transition from localized high pore pressure to a more uniform

pressure distribution (Fig. 2d). This behavior highlights a fundamental difference in hydraulic fracturing between high- and low-permeability reservoirs. Moreover, the saturation evolution confirms that the proposed method effectively captures the unstable displacement of $scCO_2$ in saline aquifers.

Overall, $scCO_2$ transport evolves from a fracturing-dominated regime at early times to an infiltration-fracturing competitive regime, and ultimately to an infiltration-dominated regime once fracture growth stabilizes (Huang et al., 2012). This mechanism offers key insights into $CO_2$sequestration in high-permeability formations, where fracture growth is often considered detrimental due to leakage risks. By appropriately regulating injection parameters to control the stabilized fracture length, storage efficiency can be substantially enhanced without compromising containment security.

## 3.3 Parameter analysis

The temporal evolution of the three transport regimes arises from the competition between $scCO_2$ migration and fracture propagation. Similar regime transitions are also observed across the parameter space under different injection conditions and fluid properties. In this study, five injection rates are considered. To isolate the effect of $scCO_2$ viscosity, three temperature conditions (56.3°C, 47.4°C, and 37.9°C) are selected at the pore pressure of 10MPa, corresponding to viscosities of 2.44e-5,3.08e-5, and 5.21e-5Pa·s, and densities of 313.69, 433.32, and 666.63 kg/m$^3$, respectively (Span and Wagner, 1996). The detailed simulation settings are summarized in Fig. 3. Temperature-dependent variations in the properties of the background fluid and the solid matrix are neglected.

Fig. 3 shows the $scCO_2$ saturation distributions when the plume reaches computational boundary under different conditions. Increasing injection rate drives a transition of $scCO_2$ transport from infiltration-dominated to fracturing-dominated pattern. At low injection rates, pressure is primarily dissipated by matrix seepage and remains below the breakdown pressure, preventing fracture initiation (A1-A3); $scCO_2$ transport is therefore infiltration-dominated. As the injection rate increases, infiltration can no longer fully relieve pressure, and fractures initiate once the breakdown pressure is exceeded (B1-B3). Because infiltration and breakdown pressures are comparable in this regime, fracture growth is limited, pressure decreases, seepage boundaries expand, and transport reverts to infiltration dominance.

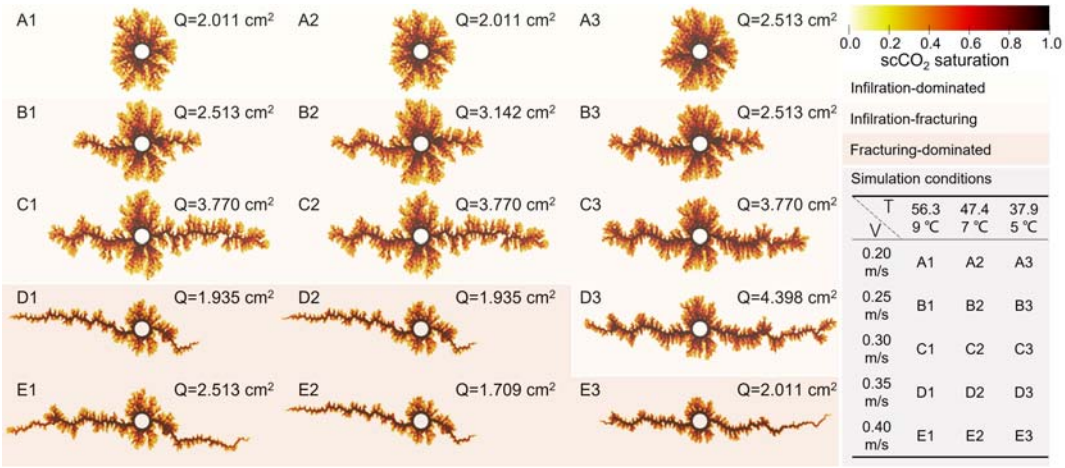



Fig. 3The $scCO_2$plume distributions governed by the competition fracturing and infiltration under different conditions. Q denotes the thickness-normalized injected $scCO_2$ volume.

At higher injection rates, infiltration and fracture propagation remain in sustained competition over larger spatial and temporal scales, enabling rapid $scCO_2$ migration over extended regions (C1-C3, D3). In case D3,this balance maximizes the injected $scCO_2$ volume, reaching $Q$=4.398cm$^2$as the $scCO_2$ plume approaches the boundary. At excessively high injection pressures, fracture propagation dominates, allowing $scCO_2$ to reach the boundary rapidly and reducing the retained injected volume. These results indicate that maintaining comparable infiltration and breakdown pressures through injection-rate control promotes sustained competition, enabling fast yet controllable $scCO_2$ injection and storage.

In addition, temperature-induced viscosity reductions markedly affect the $scCO_2$ plume distribution. Comparing cases A1 and A3, the outer region of the plume in A1 exhibits lower $scCO_2$ saturation, indicating more pronounced incomplete displacement. Consequently, at the same injection rate, lower-viscosity $scCO_2$ reaches the upper and lower boundaries earlier, while the retained injected volume is

reduced. Viscosity variations also exert a strong influence on fracture morphology. Although fractures are theoretically expected to propagate parallel to the x-direction (e.g., E3), reduced $scCO_2$ viscosity produces more tortuous and localized fracture paths that are increasingly sensitive to rock heterogeneity. Enhanced infiltration further promotes local reductions in effective stress within mechanically weak zones. These observations suggest that lower viscosity is a key factor driving the increased complexity and tortuosity of fracture networks during $scCO_2$ injection compared with conventional hydraulic fracturing.

# 4 Conclusions

This study proposes a micro-continuum VOF-BPM framework for simulating hydro-mechanical coupling in weakly cemented sandstones during $scCO_2$ injection. A semi-implicit hydro-mechanical coupling algorithm is developed, enabling hydraulic fracture simulation within a micro-continuum-based CFD-DEM approach. Three $scCO_2$ transport regimes are identified: infiltration-dominated, infiltration-fracturing competitive, and fracturing-dominated. The results demonstrate increasing injection rate drives a transition from infiltration-controlled transport to fracture-dominated flow, while optimal injection and sequestration efficiency occurs at moderate rates where sustained infiltration-fracturing competition persists over extended space and time. Reduced $scCO_2$ viscosity promotes more tortuous and localized fracture networks and enhances unstable displacement, potentially limiting storage capacity. Overall, the proposed framework bridges discrete and continuum approaches in hydro-mechanical coupling and provides a robust tool for mesoscale multiphysics simulations in heterogeneous geomaterials.

# References

Carrillo, F.J., Bourg, I.C., Soulaine, C., (2020). Multiphase flow modeling in multiscale porous media: An open-source micro-continuum approach. Journal of Computational Physics: X 8, 100073. https://doi.org/10.1016/j.jcpx.2020.100073

Goniva, C., Kloss, C., Deen, N.G., Kuipers, J.A.M., Pirker, S., (2012). Influence of rolling friction on single spout fluidized bed simulation. Particuology 10, 582–591. https://doi.org/10.1016/j.partic.2012.05.002

Huang, H., Zhang, F., Callahan, P., Ayoub, J., (2012). Granular Fingering in Fluid Injection into Dense Granular Media in a Hele-Shaw Cell. Phys. Rev. Lett. 108, 258001. https://doi.org/10.1103/PhysRevLett.108.258001

Kazidenov, D., Amanbek, Y., (2025). CFD-DEM modeling of fracture initiation with polymer injection in granular media. Particuology 97, 58–68. https://doi.org/10.1016/j.partic.2024.12.001

Li, M., Zhang, F., Wang, S., Dontsov, E., Li, P., (2024). DEM Modeling of Simultaneous Propagation of Multiple Hydraulic Fractures Across Different Regimes, from Toughness- to Viscosity-Dominated. Rock Mech Rock Eng 57, 481–503. https://doi.org/10.1007/s00603-023-03554-2

Parisio, F., Vilarrasa, V., Wang, W., Kolditz, O., Nagel, T., (2019). The risks of long-term re-injection in supercritical geothermal systems. Nat Commun 10, 4391. https://doi.org/10.1038/s41467-019-12146-0

Potyondy, D.O., Cundall, P.A., (2004). A bonded-particle model for rock. International Journal of Rock Mechanics and Mining Sciences, Rock Mechanics Results from the Underground Research Laboratory, Canada 41, 1329–1364. https://doi.org/10.1016/j.ijrmms.2004.09.011

Schramm, M., Tekeste, M.Z., Plouffe, C., Harby, D., (2019). Estimating bond damping and bond Young's modulus for a flexible wheat straw discrete element method model. Biosystems Engineering 186, 349–355. https://doi.org/10.1016/j.biosystemseng.2019.08.003

Snæbjörnsdóttir, S.Ó., Sigfússon, B., Marieni, C., Goldberg, D., Gislason, S.R., Oelkers, E.H., (2020). Carbon dioxide storage through mineral carbonation. Nat Rev Earth Environ 1, 90–102. https://doi.org/10.1038/s43017-019-0011-8

Soulaine, C., Tchelepi, H.A., (2016). Micro-continuum Approach for Pore-Scale Simulation of Subsurface Processes. Transp Porous Med 113, 431–456. https://doi.org/10.1007/s11242-016-0701-3

Span, R., Wagner, W., (1996). A New Equation of State for Carbon Dioxide Covering the Fluid Region from the Triple-Point Temperature to 1100 K at Pressures up to 800 MPa. Journal of Physical and Chemical Reference Data 25, 1509–1596. https://doi.org/10.1063/1.555991

Van Genuchten, M.Th., (1980). A Closed-form Equation for Predicting the Hydraulic Conductivity of Unsaturated Soils. Soil Science Soc of Amer J 44, 892–898. https://doi.org/10.2136/sssaj1980.03615995004400050002x